Increasing the Insertion Loss of Sonic Crystal Noise Barriers with Helmholtz Resonators

Javier Redondo [1,*], David Ramírez-Solana [1,2] and Rubén Picó [1]

1   Instituto de Investigación para la Gestión Integrada de Zonas Costeras, Universitat Politècnica de València, Campus de Gandía, C. Paranimf, 1., 46730 Gandía, Spain
2   Dipartimento di Ingegneria Elettrica e dell'Informazione, Politecnico di Bari, Via Orabona, 4, 70125 Bari, Italy
*   Correspondence: fredondo@fis.upv.es

Abstract: Helmholtz resonators (HRs) have the advantage of extending and improving their insulating capacity when used as scatterers in noise barriers made of periodic media, such as sonic crystals (SCs). However, the interaction between multiple Bragg scattering and local resonance phenomena can increase or decrease the insulation of the barrier depending on its design. In the present work, we numerically investigate the factors that determine how such interferences occur and the specific conditions to increase the insertion loss of sonic crystal noise barriers (SCNBs) made of cylindrical scatterers with HRs. Two factors are crucial for the variation of the isolation of the barrier in the Bragg-bandgap (Bragg-BG): the orientation of the resonator mouth with respect to the incident wave, and the resonance frequency of the resonator with respect to the central frequency of the Bragg-BG. Based on this phenomenon, we propose a sonic crystal noise barrier consisting of scatterers with two Helmholtz resonators. The insertion loss of the structure is determined numerically and shows an increase of 20 dB at the BG compared to a conventional barrier with cylindrical scatterers.

Keywords: sonic crystals; Helmholtz resonator; noise barrier; numerical methods; FDTD

1. Introduction

A major problem in today's industrialized world is noise and its effects on people's health. Various solutions have been proposed to solve this problem using noise reduction techniques, which are applied at three different stages: near the source, at the transmission, and at the receiver. The most common solution, and the most widely used because of its simplicity, is the use of devices at the transmission level or, more precisely, the installation of noise barriers (NBs) between the source and the receiver [1]. The insulation performance of NB can be improved by a suitable choice of shape: the geometry of the edge or the curvature of the main flat surface can be designed to modify the diffraction of the upper part [2]. Incorporating porous materials into them also helps to improve their acoustic perfor-mance, especially with regard to the reflection of sound waves between the source and body of the NB [3].

In this field, a new method has emerged in the last decades, which has new properties in contrast to conventional flat walls for noise reduction: sonic crystal noise barriers (SCNB) [4–8]. SCNBs are made of periodic materials called sonic crystals, which are arrays of scatterers embedded in air [9]. While conventional barriers do not allow air or water to pass through, SCNBs are permeable to fluids. Moreover, they can be arranged to attenuate noise in specific target frequency ranges, which is one of their advantages over conventional barriers that cannot distinguish between different noises. SCNBs exhibit the property of Bragg bandgaps (Bragg-BGs), with frequency ranges for which acoustic waves are not able to propagate due to the interference generated by the multiple scattering of waves [10–12]. The central frequency of the first Bragg-BG is $f_c = c/2a$, where c is the speed of sound in the fluid (m/s), and the lattice constant (a) is the distance between scatterers and is

characteristic of the unit cell of a crystal lattice [13]. Bragg-BGs have improved the ability to control wave propagation through many additional applications, such as waveguides [14] or diffusers [15,16]. Some approaches have been developed to improve the insulation level and range of Bragg-BGs, e.g., by using fractal geometries [17] or different radii of the scatterers that make up the SCs [18].

In addition to Bragg scattering, BGs are also produced by local resonances. In particular, they are used to induce low-frequency BGs in SCs and have been studied in one- two-dimensional periodic arrays [19–23]. In acoustic systems, these resonances are usually generated by Helmholtz Resonators (HRs) [24]. The BGs based on local resonances of HRs (HR-BGs) depend on the alignment of the mouth of the resonator with respect to the incident sound wave. Some studies have shown that an opposite arrangement of the HRs mouths can help to achieve sound insulation and air ventilation simultaneously [25], and that the maximum of the absorption coefficient is extremely angle dependent [26]. The HR-BG has a smaller frequency range than the Bragg-BG, but several authors have proposed to extend the BGs of SCs by multiresonant scatterers [27–32]. HR-BG and Bragg-BG influence each other [33,34] and sometimes the interaction between the two wave propagation phenomena does not improve the insulation capacity of the SCNB. [35]. As far as we know, there are no studies on the effect of this interaction on the transmission of a SCNB and on the specific influence of the resonator on the Bragg-BG. The main purpose of this work is to study the effect of the interaction between the local resonance and the Bragg interference in order to increase the noise insulation produced by SCNBs.

2. Materials and Methods

The development and validation of innovative solutions for noise reduction usually requires an enormous amount of time, specific laboratory resources and high costs with little scope for change until a new prototype is manufactured. To circumvent these drawbacks, the scientific community has developed and validated several numerical algorithms to evaluate the acoustic performance of new devices, as it is crucial to accurately predict their acoustic properties even before they are designed. These simulation techniques have contributed to the advancement of acoustic technology, especially to the development of novel periodic materials, such as SCs. These numerical simulation techniques, in combination with optimization strategies, are efficient design tools as they allow the development of devices with improved acoustic performance and new features [15,16,36].

The periodicity and symmetries of SCs allow the calculation of the model to be simplified and to achieve an approximation to the real case of long domains with high accuracy, e.g., the evaluation of the insulation solution for an extended path, such as highways or railways. In recent years, a variety of simulation methods have been used to evaluate the effectiveness of periodic structures in acoustics. In the present work, domain-discretized techniques are used for numerical simulations.

2.1. The Finite-Difference Time-Domain (FDTD) Method

The FDTD method uses finite differences as approximations for the spatial and temporal derivatives of the fundamental equations. The method was first proposed by K. Yee for electromagnetics [37]. Maloney and Cummings [38] adapted the method to the field of acoustics by converting the momentum conservation and continuity equations into central difference equations, thus obtaining updated formulas for acoustic pressure and particle velocity. The seminal work of Cao et al. showed how efficient FDTD works for band structure calculations [39], and Miyashita focuses on the study of waveguides based on SCs [14]. FDTD has also been used in recent work on sonic crystals [15,16,40–42]. According to the work of Peiró-Torres et al. [43], FDTD is not the best method to determine the insertion loss of a SC due due to the ratio between computational cost (memory) and accuracy. The high memory requirement is the main disadvantage of volumetric methods, such as FEM and FDTD. However, in terms of computation time, FDTD stands out from other methods, such as BEM and FEM, because it is a time-domain method that can cover a

large frequency range with a single simulation. To ensure the stability of the method, the Courant–Friedrichs–Lewy number must not be greater than 1 [44]. Moreover, this number should be as high as possible to minimize numerical dispersion, i.e., numerical error in phase velocity.

As with other numerical methods, in FDTD there is a limit to the maximum frequency that can be correctly simulated, which is related to the size of the mesh elements, also known as the spatial step. The typical rule of thumb is 8 elements per wavelength. However, since the numerical model, in this case, contains circular geometries (cylindrical scatterers), it is preferable to define finer meshes to avoid the need to apply conformal methods to minimize the staircase effect. In this work a mesh with square structure has been used.

2.2. Numerical Model

We consider a two-dimensional SC, which consists of a set of HRs distributed in an infinite square periodic lattice. Figure 1a shows the unit cell of the two-dimensional periodic system under investigation, which is defined by a scatterer with the outer radius R and a HR inside. Periodic boundary conditions are set at the X and Y boundaries so that the infinitely extended SC is defined by a periodic structure with a square lattice and a lattice constant (a) defining the unit cell. The irreducible Brillouin zone is also shown and represents the central cell of the reciprocal lattice. In a two-dimensional system, the filling fraction is the ratio between the area occupied by the scatterer and the area of the entire unit cell. The resonator is characterized by the length of the neck (*L*), the width of the mouth (*w*), and the inner surface area (S = πr^2), where *r* is the inner radius of the surface of the HR. The first resonance frequency of the resonator is [24]:

$$f_{HR} = \frac{c}{2\pi}\sqrt{\frac{w}{\left(L + \Delta\frac{w}{2}\right)S}} \, , \tag{1}$$

where Δ is the correction factor for neck length added account for the effects of the neck-cavity junction caused by a sudden change in the circular cross-sections (usually between 1.6 and 1.8) [45]. For simplicity, the geometry of the resonator for all the simulations in this work was chosen to neglect the viscothermal losses in the medium (see Appendix A).

The band structure describes the dispersion relation of waves in the SC. FDTD simulations were used to calculate the band structure. In the band structure, propagation bands and BGs can be identified. In this work, we are interested in two propagation directions: 0° and 90°. The band structure is calculated in the two corresponding directions in reciprocal space or k-space: 0° (ΓX) and 90° (ΓX'), where G ($k_x = 0$, $k_y = 0$), X ($k_x = \pi/a$, $k_y = 0$) and X' ($k_x = 0$, $k_y = \pi/a$) denote the boundaries of the first Brillouin zone. Numerical simulations using the FDTD method are performed to evaluate the transmission of two SCNBs with a design based on the unit cell defined in Figure 1a. Periodic Boundary Conditions (PBC) are considered to reproduce an infinite SC in the Y-direction but truncated to three layers of scatterers in the X-direction (see Figure 1b,c). Since our SC has square symmetry, the periodicity is the same in the *x*- and *y*-axis, and in the two transmission models, both the distance between the scatterers and the transverse dimension (*y*-axis) of the models are a = 17 cm, with a filling fraction ff = π (r/a)2 = 0.4. This means that the external radius (R) is 6.86 cm and the distance between the scatterers is a/2-R = 1.64 cm.

Thus, the geometric model of the SCNBs and the unit cell have the same topology, namely a two-dimensional square-periodic structure. An incident plane wave with frequency f and acoustic pressure P_i propagates along the *x*-axis from left to right in such a way that it is aligned with the mouth of the HR in Figure 1b and perpendicular to it in Figure 1c (hereafter referred to as the 0° and 90° alignments). Perfectly Matched Layers (PMLs) are applied to both *x*-axis boundaries in the models to absorb waves propagating outward from the domain.
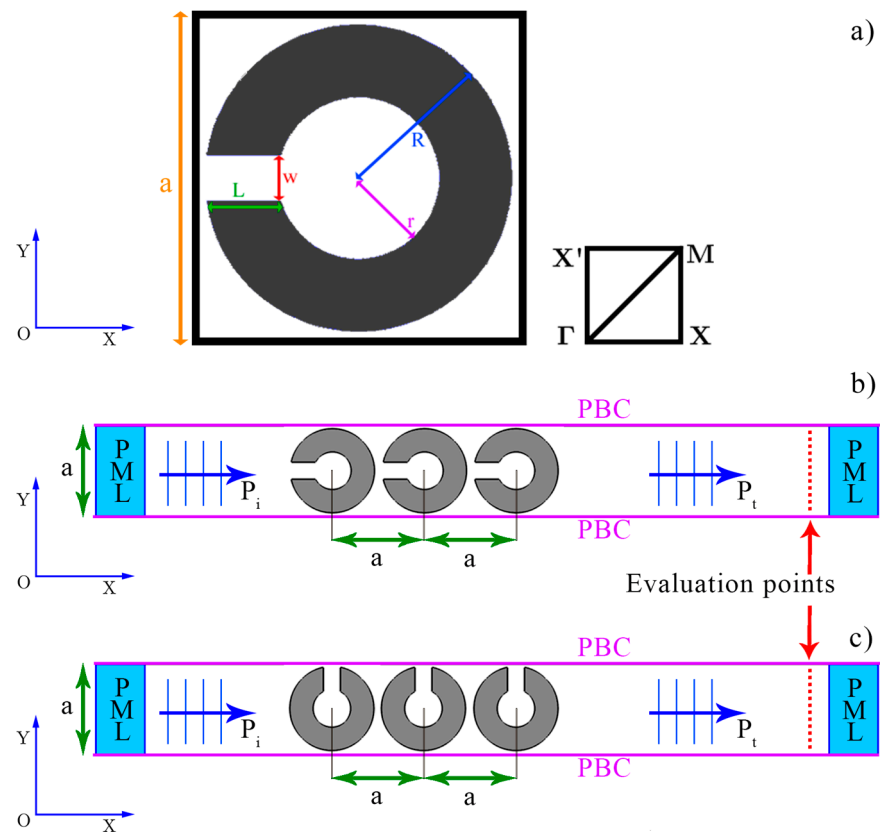
Figure 1. (**a**) Unit cell of the two-dimensional scatterer with HR, which forms the periodic system defining the SC and irreducible Brillouin zone of the square lattice SC based on the Bloch–Floquet theory for the calculation of the band structure. Numerical models for the SNCBs with 3-rwo scatterers for the evaluation of the IL with (**b**) 0° aligned and (**c**) 90° aligned HRs.

The transmission of the system is analyzed in the evaluation points of a line at a distance of 1 m from the SC by evaluating the transmission coefficient (τ) defined by:

$$\tau = \frac{< P_t^2 >}{< P_i^2 >},$$

(2)

where <·> stands for the averaging of both, the squared incident acoustic pressure and the squared transmitted acoustic pressure (P_t) at the evaluation points. From τ the equation for the Insertion Loss (IL) in decibels can be derived as follows:

$$\text{IL} = -10 \times \log_{10}(\tau) \ [\text{dB}],$$

(3)

and indicates how the sound pressure level at the evaluation points changes when the SCNB is positioned in the acoustic path of the incident wave.

3. Bragg and Helmholtz Resonances Interaction

The effect of multiple scattering interference significantly reduces the transmission of a SCNB in the BGs and increases its insulation. In general, this phenomenon applies not only to the Bragg-BG, but also to the HR-BG [20]. In the model proposed here, the scatterers have a local resonator. Depending on the central frequencies and the width of their BGs, both Bragg-BG and HR-BG can overlap, leading to a different type of interaction between the phenomena [33,34].

Next, the transmission of an incident plane wave from a SCNB is investigated numerically using the models shown in Figure 1b for the 0° alignment and Figure 1c for the 90° alignment. The aim is to analyze the physical interaction between the first Bragg

resonance and the first local resonance and their mutual interaction. The value of the specific central frequency of the HR-BG influences the width and the insulation of the Bragg-BG. Two SCNBs are studied with their HR-BG below and above the Bragg-BG with a fixed lattice constant (a = 0.17 m), i.e., a central Bragg frequency of fc = 1000 Hz. According to (1), the HR resonance frequency depends on the neck, the mouth, and the surface of the two-dimensional resonator. The resonant frequency of the HR could be changed by suitably varying each of these parameters according to (1). However, due to geometric constraints in the design of the resonator inside the scatterer, it is appropriate to vary the surface of the resonator to cover a wide range of HR resonant frequencies with realistic geometries. Figure 2 shows results of FDTD simulations of the transmission coefficient of a SCNB in a solid line based on the models shown in Figure 1b,c together with the band structure of the SC, with circles with 0° alignment in red and 90° alignment in blue for ΓX and ΓX′, respectively. For reference, the SCNB is shown with Closed Cylinders, SCNB-CC, i.e., without local resonance, in black. The scatterers of the SCNB have a HR with a mouth w = 1 cm, a neck L = 1 cm, and an r = 4.5 cm, corresponding to a resonant frequency f_{HR} = 400 Hz < fc. The frequency range includes the first Bragg-BG with the central frequency f_c and the first HR-BG, with resonance frequency f_{HR}. Both phenomena have higher resonances, but they are far from interacting with the first resonances and their mutual interactions are beyond the scope of this work.
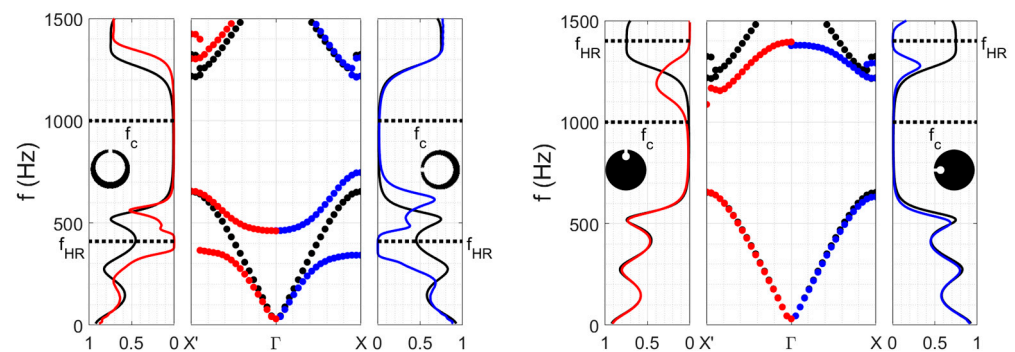
Figure 2. Transmission coefficient of the SCNB and band structure of the corresponding SC with (**left**) f_{HR} < fc and (**right**) f_{HR} > fc of the configurations with 0° alignment (blue) and 90° alignment (red). The SCNB-CC case is plotted in black for reference.

Although the band structure was obtained from an infinite periodic SC and the transmission loss from the SCNB with an array of three layers of resonators, the agreement between the presence of BGs and transmission minima is significant. Figure 2-left shows the case of a HR with a small surface and, thus, a resonant frequency lower than the central frequency of the Bragg-BG (f_{HR} < fc). At low frequencies, below and around the local resonance, oscillations are observed in the transmission, which are due to Fabry–Perot interference phenomena [46] due to the multiple reflections of the waves at the truncated ends of the SC. This is thus a phenomenon caused by the finite length of the crystal and cannot be explained by the band structure of the infinite SC. The interaction between the two BGs is visible in the frequency range of the HR-BG below the Bragg-BG, where the greatest difference from the case of the SCNB-CC is observed. A significant reduction in transmission is observed for both 0° alignment and 90° alignment due to the local resonance. Figure 2-right shows the case where the resonance frequency of the HR has been tuned above the Bragg-BG (higher surface). The scatterers of the SCNB have a HR with a mouth w = 1 cm, a neck L = 1 cm, and r = 1.2 cm, corresponding to f_{HR} = 1400 Hz > fc. Again, the reduction of the transmission coefficient can be observed in the frequency range where the local resonance and the Bragg resonance interact. In Supplementary Materials an animation shows the interaction of Bragg diffraction and the local resonance with the f_{HR} in the range from 400 Hz to 1400 Hz.

Figure 3 shows the numerical results of IL for several SCNBs consisting of arrays of HRs tuned to f_c = 1000 Hz (a = 0.17 m) in a color scale. Each sub-figure contains the results of IL for 60 numerical simulations of arrays of HRs with different resonant frequencies. The resonant frequency of the HR is plotted on the *y*-axis and the frequency of the propagating waves on the *x*-axis. For illustration, the lower and upper limits of the Bragg-BG of the SCNB-CC are drawn with vertical white dashed lines at f = 713 Hz and f = 1092 Hz, respectively (criterion IL = 18 dB). Since the phenomenon of local resonance does not occur in an SCNB-CC, the IL is identical for all SCNBs along the entire *y*-axis. The white dotted line corresponds to the value of the theoretical resonance frequency of the HR, calculated from (1). Figure 3 left shows the case of the SCNB with 0° alignment. The IL depends strongly on the resonance frequency of the HRs. The nature of the interaction between Bragg-BG and HR-BG is determined by their relative frequency resonances. When f_{HR} is far from f_c (f_{HR} < 600 Hz and f_{HR} > 1200 Hz), both resonances are well separated. When the resonances are closed (600 Hz < f_{HR} < 1200 Hz), the interaction is significant and important changes in the IL are observed with respect SCNB-CC. The IL has an asymmetric shape because the transmission is much higher at frequencies f < f_{HR} than at frequencies f > f_{HR}. For example, at f_{HR} = 1400 Hz, the Bragg-BG is similar to that of the SCNB-CC at the same frequency, which agrees quite well with the white vertical dashed lines. The interaction between the resonances of the IL of the SCNB with 90° alignment is shown in Figure 3 right. It is also asymmetric with respect to the local resonant frequency, but the insulation increase occurs at frequencies below the Bragg frequency. The increase of IL due to the interaction between the Bragg resonance and the local resonance thus strongly depends on the specific orientation of the HRs of the SCNB with respect to the incident plane wave.
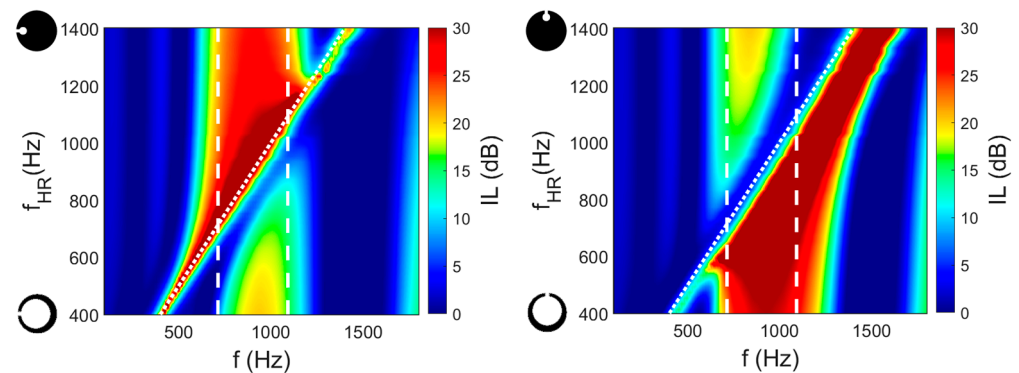
Figure 3. Insertion loss of SCNB with varying HR resonant frequency for the configuration with (**left**) 0° alignment and (**right**) 90° alignment. The dashed vertical lines represent the lower and upper Bragg-BG limits of the SCNB-CC. The value of the theoretical resonant frequency of the HR is represented by the white dotted line.

Figure 4 shows the IL as a function of frequency for specific cases with f_{HR} = 400 Hz (f_{HR} < f_c) and f_{HR} = 1400 Hz (f_{HR} > f_c) in red and blue respectively. Figure 4 left shows the 0° alignment. The SCNB-CC is shown in dashed black. The colored area visually shows the change of the IL of the SCNB with HRs with respect to the SCNB-CC. It can be observed that in the case where f_{HR} is above the Bragg-BG, the IL increases compared to the SCNB-CC. If the resonance frequency is below, the opposite is true: the insulation of the SCNB decreases. Instead, the IL decreases compared to the SCNB-CC when the f_{HR} is above the Bragg-BG, as can be seen in Figure 4 right for a 90° alignment. The IL of the SCNB, on the other hand, increases when the resonance is below. The above results prove that the orientation of the HR mouth in a SCNB is directly related to its insulating properties. Moreover, the resonant frequency of the resonator can be tuned to increase the IL of the SCNB at the Bragg-BG by choosing the alignment of the HRs accordingly. It should be noted that the coexistence of Bragg resonances and HR resonances not only leads to an increase or decrease of IL at the Bragg-BG, but also to a frequency shift of f_c. This

is due to the phase shift produced by the HR, which can be explained by a change in the lattice constant experienced by that the wave during propagation [35].
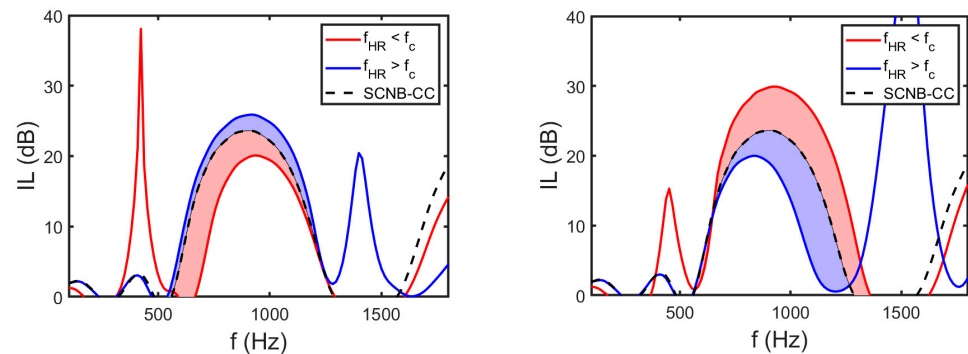
Figure 4. Insertion loss as a function of frequency of SCNBs with $f_{HR} < f_c$ (red) and $f_{HR} > f_c$ (blue) with (**left**) 0° alignment and (**right**) 90° alignment. The colored area graphically represents the variance of the IL of the SCNB with HRs with respect to the SCNB-CC (dashed black).

4. SCNB Scatterer with Two HRs

As a result of the interaction between the Bragg resonance and the local resonances, the increase in insulation of the SCNB depends strongly on the alignment of the mouth of the HR. The relative value of the local resonance (f_{HR}) with respect to the central frequency of the Bragg-BG (f_c) is an important factor as it determines the interaction between the two phenomena. The use of resonators in SCNBs does not necessarily increase their sound insulation. Therefore, careful attention should be paid to the alignment of the mouths and the resonant frequencies of the HRs in the scatterers of SCNBs. Figure 5 shows a scatterer for a SCNB consisting of two HR aligned at 0° and 90°, with variable and coupled surfaces. The inner moving wall can be rotated by an angle θ, and simultaneously changes the resonances of the two HRs. Both HR have identical mouths w = 3 cm and L = 1.5 cm. As in Section 3, IL is computed numerically in a SCNB consisting of scatterers arranged in a two-dimensional square lattice with a filling fraction ff = 0.4 and the central frequency of the Bragg-BG is f_c = 1000 Hz.
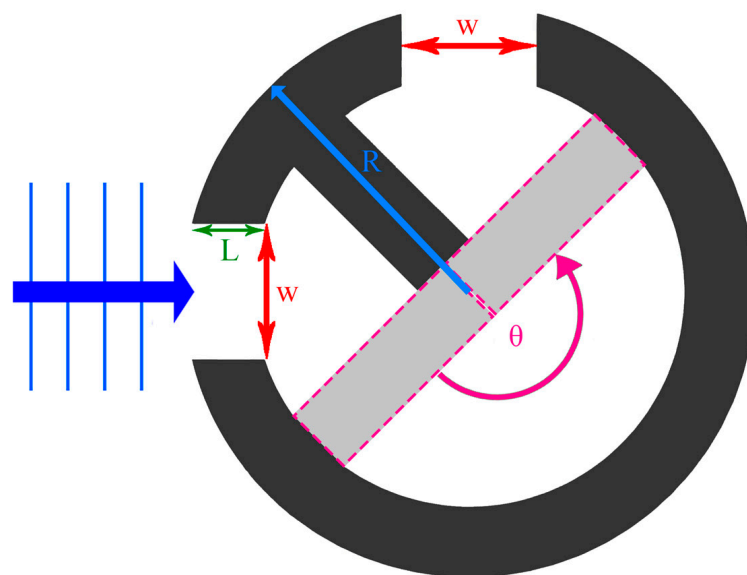
Figure 5. Cylindrical scatterer consisting of two HRs with identical mouth and variable coupled surfaces through a rotating inner wall.

Figure 6 shows the behavior of a SCNB with cylinders with two HRs and the influence on the IL due to the movement of the inner moving wall. Figure 6 left shows the IL in color scale for the SCNB with scatterers with coupled HRs as a function of the rotation angle θ of the wall analyzed with the same numerical model as in Figure 1b,c. The change in SCNB insulation behavior results from θ-driven surfaces changes in the HRs. Thus, if the HR with 0° alignment has a smaller surface (θ = 0°), the HR with 90° alignment has the largest surface and the IL in the BG-Bragg is high. However, the surfaces ratio of the HRs is changed, IL varies. When the surfaces of the HRs are inverted (θ = 180°), the IL in the BG-Bragg decreases drastically and only the resonances of the respective HRs are observed. HRs do not behave the same with identical surfaces due to the uneven alignment of their mouths in relation to the incident wave. This asymmetry favors the increase of the insulation of the structure when frequencies of the HRs are properly tuned for each alignment.
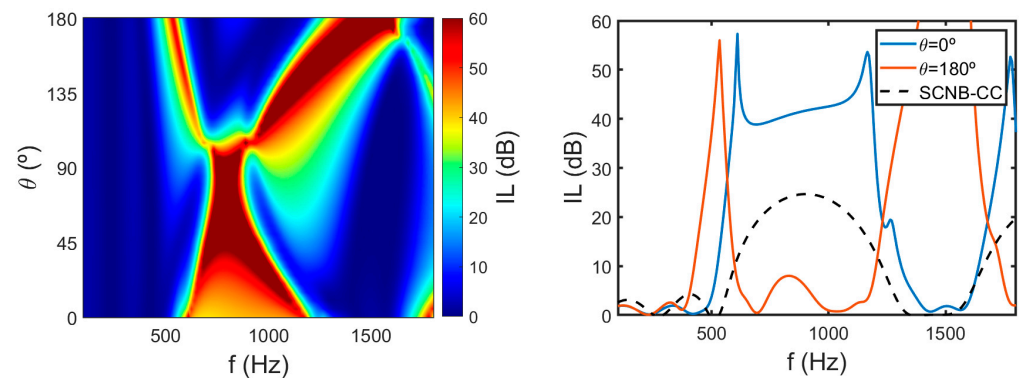
Figure 6. (**Left**) IL in color scale as a function of frequency for SCNB with scatterers with coupled-surface HRs as a function of the inner wall rotation angle. (**Right**) Cases θ = 0° and θ = 180° and SCNB-CC.

Figure 6 right shows the IL as a function of frequency for the cases θ = 0°, θ = 180° and the SCNB-CC. As seen in Section 3, the IL of SCNB at the Bragg-BD increases in 0° alignment for $f_{HR} < f_c$ and decreases in 90° alignment for $f_{HR} > f_c$. This condition is fulfilled for both coupled-surface HRs when θ = 0°. In this case, the surface of the HR with 0° alignment is actually minimum and the surface of the 90° alignment is maximum. It can be seen that the frequency range corresponding to the Bragg-BG (between 500 Hz and 1300 Hz), the IL increases by about 20 dB compared to the SCNB-CC due to the interaction between Bragg and local resonances. The central frequencies of HR-BG of both HRs appear as local maxima in the IL at f = 610 Hz and f = 1165 Hz for the HR aligned at 90°. In this configuration, the resonators have resonance frequencies at the edges of the Bragg-BG. The interaction between the local resonances and the Bragg resonance leads to a reduction in the transmission of the SCNB or, in other words, an increase in the insertion loss. When the inner wall is rotated to θ = 180°, the surfaces of the HRs are reversed and the acoustic behavior of the SCNB changes drastically. The IL of the Bragg-BG changes by more than 30 dB when the wall is rotated from θ = 0° to θ = 180° and the resonance frequencies now shift to f = 534 Hz and f = 1520 Hz. Although both configurations are geometrically equivalent because their HRs have identical surfaces, the central frequencies of the HR resonances are different because of the different alignment of the cylinders with respect to the incident wave.

As Figure 6 right shows, the IL reaches SPL = 40 dB in the Bragg-BG frequency range. In [27], the combination of concentric closed-cylinders and cylinders with HR gives numerical and experimental results with less than 20 dB in the Bragg-BG frequency range. Several settings of HRs scatterers have been tested numerically and experimentally in [23], including porous materials inside the cylinder, but none of the combinations brought more than 25 dB in the whole Bragg-BG frequency range. Thus, our proposal of a barrier with

resonators tuned at the edges of Bragg-BG offers a very significant increase in IL compared to other proposals in the literature.

Since SC is not an isotropic material, the acoustic behavior of SCNB with other incidences may be considered. This approach is made considering that the noise source is far away enough, so when source is closer, it would be interesting analyze how the SCNB performs. Instead of rotating the separator of the two HR cavities, rotate the whole cylinder can be also a good choice. By doing this, each scatter will have two different degrees of freedom. Implementing automatic control according to different stimulus could also be an extremely complex and versatile system, with the adaptative ability to perform several cases. Another interesting prospect to study would be now explore periodical configurations and see how the resonant scatterer performs.

5. Conclusions

The insulation of a SCNB with HRs was analyzed for different configurations and orientations with respect to the incident wave. The interaction between local resonance and Bragg interference phenomena and the alignment of the mouth with respect to the incident wave is crucial for the design of SCNB with high insulation capacity. When the orientation of the HR aligns with the incident acoustic wave, the transmission of the barrier is reduced if the local resonant frequency is lower than the Bragg-BG. IL also becomes higher when it is perpendicular to the incident wave and the local resonant frequency is higher than the Bragg-BG. Based on this mechanism, a cylindrical scatterer composed by two HRs is proposed, which increases the insertion loss of a SCNB by up to 20 dB compared to a NB made of closed cylinders.

Supplementary Materials: The following supporting information can be downloaded at: https://www.mdpi.com/article/10.3390/app13063662/s1, Video S1: Band Structure FDTD.

Author Contributions: Conceptualization, J.R.; methodology, J.R., D.R.-S. and R.P.; software, J.R. and D.R.-S.; validation, J.R. and R.P.; formal analysis, J.R. and R.P.; investigation, J.R., D.R.-S. and R.P.; resources, J.R. and R.P.; data curation, J.R., D.R.-S. and R.P.; writing—original draft preparation, J.R. and D.R.-S.; writing—review and editing, J.R., D.R.-S. and R.P.; visualization, D.R.-S.; supervision, J.R. and R.P.; project administration, R.P.; funding acquisition, J.R. and R.P. All authors have read and agreed to the published version of the manuscript.

Funding: This work was supported by the Spanish Ministry of Economy and Innovation (MINECO) and the European Union FEDER (project PID2019-109175GB-C22).

Institutional Review Board Statement: Not applicable.

Informed Consent Statement: Not applicable.

Data Availability Statement: The data presented in this study are available on request from the corresponding author.

Acknowledgments: Authors acknowledge the Sonic Crystals Technologies research group for encouraging us to write this paper.

Conflicts of Interest: The authors declare no conflict of interest.

Appendix A

This appendix explains why viscothermal losses do not necessarily need to be considered in the modelling in the numerical simulations in this paper. To this end, a model of viscothermal losses is presented and verified by numerical simulations that its acoustic effects are negligible compared to an equivalent lossless system. The main causes of dissipation of acoustic energy in a SCNB with HR are viscous forces and thermal conduction, which occur mainly at the viscous and thermal boundary layers. Temperature and velocity gradients between the bulk domain and the boundary surface are responsible for the losses. Based on these mechanisms, a distinction can be made between a thermal and a viscous boundary layer. While the heat gradient occurs when this boundary wall is isothermal, the

velocity gradient can be explained by the fluid viscosity (μ) and the no slip condition at the wall. While the thermal boundary layer (δ_t) is a function of the fluid thermal conductivity (κ), the viscous boundary layer (δ_v) is dependent on the fluid viscosity. According to the following equations, the boundary layers are both frequency dependent [47]:

$$\delta_t = \sqrt{\frac{\kappa}{\rho_0 C_p \, \pi f}} \, , \tag{A1}$$

and

$$\delta_v = \sqrt{\frac{\mu}{\rho_0 \, \pi f}} \, , \tag{A2}$$

where C_p is the fluid heat capacity at constant temperature and the fluid density is ρ_0. Both characteristic lengths are related according to the not dimensional Prandtl number, $\mathrm{Pr} = (\delta_v / \delta_t)^2$.

In this study the fluid is air with T = 20° C and p = 1 atm, where thermal and viscous losses are almost equally important, having a Pr = 0.7, in contrast with water or other fluids where the role of thermal losses is smaller. Modelling viscothermal losses in acoustics can be computationally expensive as a large amount of detail is required to capture all physical effects. However, if the acoustic waves travel through slits with constant cross-section much smaller than the acoustic wavelength and larger than the thickness of the boundary layers, the viscothermal losses can be estimated by including them in the fluid in a homogenized approach for the narrow domain of the slit using the Low Reduced Frequency models [32,48].

According to the analyzed domain of the slit, the case of this study is the neck of the Helmholtz resonator embedded in the scatter and the governing equations in that zone to estimate viscothermal losses are, the complex wavenumbers by splitting it into the viscous and thermal parts, the following wavenumbers are obtained:

$$k_v{}^2 = -\mathrm{i}2\pi f \frac{\rho_0}{\mu} \, , \tag{A3}$$

and

$$k_t{}^2 = -\mathrm{i}2\pi f \frac{\rho_0 C_p}{\kappa} \, . \tag{A4}$$

As can be seen in (A1) and (A2), the viscous and thermal layers have a greater width for long wavelengths. Therefore, if their influence is negligible at low frequencies, this will also be the case at higher frequencies. For this reason, only the case where HR is tuned to low frequency is considered here to prove that viscoelastic losses can be neglected in this work. Figure A1, shows two scatterers with embedded HR. Figure A1-left shows the HR used on the work with a neck of w = 1 cm and L = 1 cm, called HR1 and Figure A1-right, the HR2 with the same theoretical resonance frequency f_{HR} = 400 Hz, the same length of the neck L = 1 cm and consequently a thinner mouth (w = 0.2 cm).

The IL of two 3-row SCNBs with both HR1 and HR2 are calculated numerically using the model presented in Section 2.2. It is shown that the viscothermal losses for the HR studied in this work can be neglected in the working frequency range. Figure A2 illustrates the IL in the frequencies of the HR-BG. Since the mouth of the resonator is quite large, no significant viscothermal losses occur in the neck of HR1. However, when the size of the mouth is reduced, the losses are no longer negligible and the acoustic properties of the SCNB change significantly. For HR2, the peak of the resonance shifts from 400 Hz to 378 Hz when viscothermal losses are taken into account. Since the acoustic model used in this work is not scalable, the results shown in this paper only apply to geometries where the viscothermal losses are negligible.
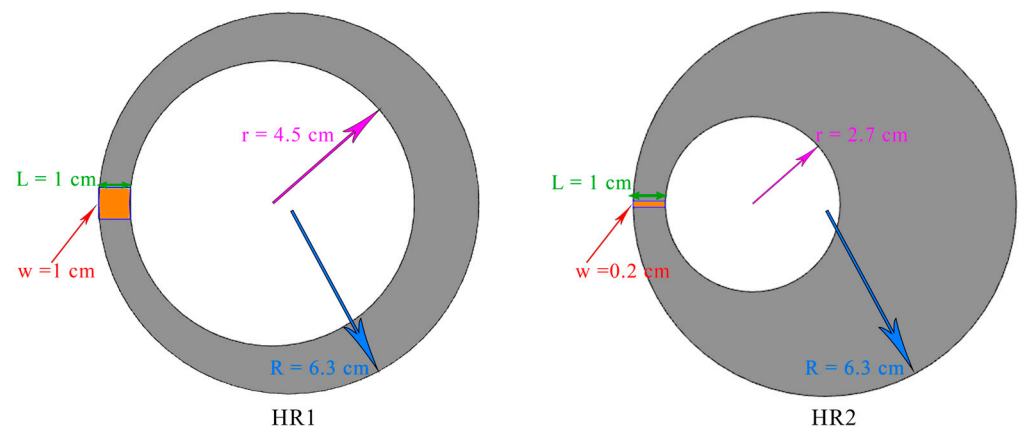
Figure A1. Left: Scatterer with HR with wider mouth (w = 1 cm) and. **Right**: Scatterer with HR with narrower mouth (w = 1 cm). HR1 and HR2 have the same resonance frequency f_{HR} = 400 Hz.
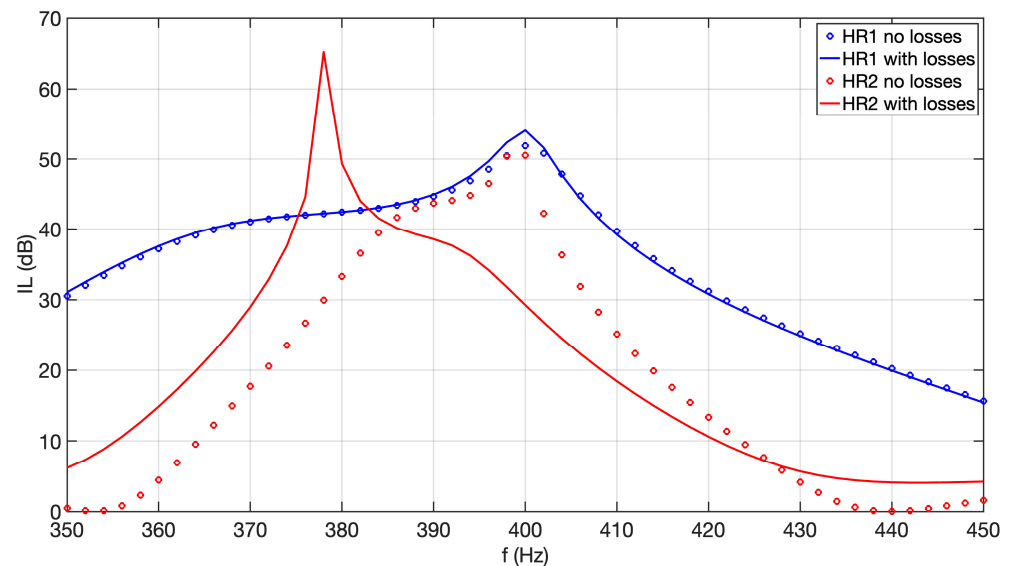
Figure A2. IL of a SCNB with HR1, used in the paper (blue) and with HR2, with a thin mouth (red) with (continuous) and without (circles) losses.

References

1. Harris, C.M. *Handbook of Acoustical Measurements and Noise Control*; McGraw-Hill: New York, NY, USA, 1991; pp. 3019–3020.
2. Branco, F.J.F.G.; Godinho, L.; Tadeu, A. Acoustic Insertion Loss Provided by Rigid Acoustic Barriers of Different Shapes. *J. Comput. Acoust.* **2003**, *11*, 503–519. [CrossRef]
3. Lázaro, J.; Pereira, M.; Alves Costa, P.; Godinho, L. Performance of Low-Height Railway Noise Barriers with Porous Materials. *Appl. Sci.* **2022**, *12*, 2960. [CrossRef]
4. Sanchez-Perez, J.V.; Rubio, C.; Martinez-Sala, R.; Sanchez-Grandia, R.; Gomez, V. Acoustic barriers based on periodic arrays of scatterers. *Appl. Phys. Lett.* **2002**, *81*, 5240–5242. [CrossRef]
5. Kushwaha, M.S. Stop-bands for periodic metallic rods: Sculptures that can filter the noise. *Appl. Phys. Lett.* **1997**, *70*, 3218–3220. [CrossRef]
6. Iannace, G.; Ciaburro, G.; Trematerra, A. Metamaterials acoustic barrier. *Appl. Acoust.* **2021**, *181*, 108172. [CrossRef]
7. Montiel, F.; Chung, H.; Karimi, M.; Kessissoglou, N. An analytical and numerical investigation of acoustic attenuation by a finite sonic crystal. *Wave Motion* **2017**, *70*, 135–151. [CrossRef]
8. Morandi, F.; Miniaci, M.; Marzani, A.; Barbaresi, L.; Garai, M. Standardised acoustic characterisation of sonic crystals noise barriers: Sound insulation and reflection properties. *Appl. Acoust.* **2016**, *114*, 294–306. [CrossRef]
9. Martínez-Sala, R.; Sancho, J.; Sánchez-Pérez, J.V.; Gomez, V.; Llinares, J.; Meseguer, F. Sound attenuation by sculpture. *Nature* **1995**, *378*, 241. [CrossRef]
10. Sigalas, M.; Economou, E. Elastic and acoustic wave band structure. *J. Sound Vib.* **1992**, *158*, 377–382. [CrossRef]
11. Kushwaha, M.S.; Halevi, P.; Dobrzynski, L.; Djafari-Rouhani, B. Acoustic band structure of periodic elastic composites. *Phys. Rev. Lett.* **1993**, *71*, 2022–2025. [CrossRef]

12. Chen, Y.-Y.; Ye, Z. Theoretical analysis of acoustic stop bands in two-dimensional periodic scattering arrays. *Phys. Rev. E* **2001**, *64*, 036616. [CrossRef] [PubMed]

13. Kittel, C. *Introduction to Solid State Physics*, 8th ed.; John Wiley & Sons, Inc.: Hoboken, NJ, USA, 2004.

14. Miyashita, T. Sonic crystals and sonic wave-guides. *Meas. Sci. Technol.* **2005**, *16*, R47. [CrossRef]

15. Redondo, J.; Picó, R.; Sánchez-Morcillo, V.; Woszczyk, W. Sound diffusers based on sonic crystals. *J. Acoust. Soc. Am.* **2013**, *134*, 4412. [CrossRef] [PubMed]

16. Peiró-Torres, M.P.; Parrilla Navarro, M.J.; Ferri, M.; Bravo, J.; Sánchez-Pérez, J.; Redondo, J. Sonic Crystals Acoustic Screens and Diffusers. *Appl. Acoust.* **2019**, *148*, 399–408. [CrossRef]

17. Castiñeira-Ibáñez, S.; Rubio, C.; Redondo, J.; Sánchez-Pérez, J.V. Quantitative characterization of bandgap properties of sets of isolated acoustic scatterers arranged using fractal geometries. *Appl. Phys. Express* **2014**, *7*, 042201. [CrossRef]

18. Ni, A.; Shi, Z. Broadband wave attenuation and topological transport in novel periodic pile barriers. *Eng. Struct.* **2022**, *262*, 114378. [CrossRef]

19. Liu, Z.; Zhang, X.; Mao, Y.; Zhu, Y.Y.; Yang, Z.; Chan, C.T.; Sheng, P. Locally Resonant Sonic Materials. *Science* **2000**, *289*, 1734–1736. [CrossRef]

20. Hu, X.; Chan, C.T.; Zi, J. Two-dimensional sonic crystals with Helmholtz resonators. *Phys. Rev. E* **2005**, *71*, 055601. [CrossRef]

21. Romero-García, V.; Sánchez-Pérez, J.V.; Garcia-Raffi, L.M. Tunable wideband bandstop acoustic filter based on two-dimensional multiphysical phenomena periodic systems. *J. Appl. Phys.* **2011**, *110*, 014904. [CrossRef]

22. Radosz, J. Acoustic performance of noise barrier based on sonic crystals with resonant elements. *Appl. Acoust.* **2019**, *155*, 492–499. [CrossRef]

23. Qin, X.; Ni, A.; Chen, Z.; Fang, M.; Li, Y. Numerical modeling and field test of sonic crystal acoustic barriers. *Environ. Sci. Pollut. Res.* **2022**, *30*, 16289–16304. [CrossRef] [PubMed]

24. Alton Everest, F.; Pohlmann, K.C. *Master Handbook of Acoustics*, 5th ed.; McGraw-Hill: New York, NY, USA, 2009.

25. Guan, Y.-J.; Ge, Y.; Sun, H.-X.; Yuan, S.-Q.; Liu, X.-J. Low-Frequency, Open, Sound-Insulation Barrier by Two Oppositely Oriented Helmholtz Resonators. *Micromachines* **2021**, *12*, 1544. [CrossRef] [PubMed]

26. Lagarrigue, C.; Groby, J.-P.; Tournat, V.; Dazel, O.; Umnova, O. Absorption of sound by porous layers with embedded periodic arrays of resonant inclusions. *J. Acoust. Soc. Am.* **2013**, *134*, 4670–4680. [CrossRef] [PubMed]

27. Mohapatra, K.; Jena, D.P. Insertion loss of sonic crystal made with multi resonant shells. *Appl. Acoust.* **2020**, *171*, 107676. [CrossRef]

28. Elford, D.P.; Chalmers, L.; Kusmartsev, F.V.; Swallowe, G.M. Matryoshka Locally Resonant Sonic Crystal. *J. Acoust. Soc. Am.* **2011**, *130*, 2746–2755. [CrossRef]

29. Romero-García, V.; Krynkin, A.; Garcia-Raffi, L.M.; Umnova, O.; Sánchez-Pérez, J.V. Multi-resonant scatterers in sonic crystals: Locally multi-resonant acoustic metamaterial. *J. Sound Vib.* **2013**, *332*, 184–198. [CrossRef]

30. Elford, D.P.; Chalmers, L.; Kusmartsev, F.V.; Swallowe, G.M. Acoustic Band Gap Formation in Metamaterials. *Int. J. Mod. Phys. B* **2012**, *24*, 4935–4945. [CrossRef]

31. Lagarrigue, C.; Groby, J.P.; Tournat, V. Sustainable sonic crystal made of resonating bamboo rods. *J. Acoust. Soc. Am.* **2013**, *133*, 247–254. [CrossRef]

32. Herrero-Durá, I.; Cebrecos, A.; Picó, R.; Romero-García, V.; García-Raffi, L.M.; Sánchez-Morcillo, V.J. Sound Absorption and Diffusion by 2D Arrays of Helmholtz Resonators. *Appl. Sci.* **2020**, *10*, 1690. [CrossRef]

33. Cenedese, M.; Belloni, E.; Braghin, F. Interaction of Bragg scattering bandgaps and local resonators in mono-coupled periodic structures. *J. Appl. Phys.* **2021**, *129*, 124501. [CrossRef]

34. Yuan, B.; Humphrey, V.F.; Wen, J.; Wen, X. On the coupling of resonance and Bragg scattering effects in three-dimensional locally resonant sonic materials. *Ultrasonics* **2013**, *53*, 1332–1343. [CrossRef] [PubMed]

35. Peiró-Torres, M.P.; Castiñeira-Ibáñez, S.; Redondo, J.; Sánchez-Pérez, J.V. Interferences in locally resonant sonic metamaterials formed from Helmholtz resonators. *Appl. Phys. Lett.* **2019**, *114*, 171901. [CrossRef]

36. Romero-García, V.; Sánchez-Pérez, J.V.; García-Raffi, L.M.; Herrero, J.M.; García-Nieto, S.; Blasco, X. Hole distribution in phononic crystals: Design and optimization. *J. Acoust. Soc. Am.* **2009**, *125*, 3774–3783. [CrossRef]

37. Yee, K. Numerical solution of initial boundary value problems involving maxwell's equations in isotropic media. *IEEE Trans. Antennas Propag.* **1966**, *14*, 302–307.

38. Maloney, J.G.; Cummings, K.E. Adaption of FDTD techniques to acoustic modelling. *11th Annu. Rev. Prog. Appl. Comput. Electromagn.* **1995**, *2*, 724–731.

39. Cao, Y.; Hou, Z.; Liu, Y. Convergence problem of plane-wave expansion method for phononic crystals. *Phys. Lett. A* **2004**, *327*, 247–253. [CrossRef]

40. Redondo, J.; Sánchez-Pérez, J.V.; Blasco, X.; Herrero, J.M.; Vorländer, M. Optimized sound diffusers based on sonic crystals using a multiobjective evolutionary algorithm. *J. Acoust. Soc. Am.* **2016**, *139*, 2807–2814. [CrossRef]

41. Pérez-Arjona, I.; Sánchez-Morcillo, V.J.; Redondo, J.; Espinosa, V.; Staliunas, K. Theoretical prediction of the nondiffractive propagation of sonic waves through periodic acoustic media. *Phys. Rev. B* **2007**, *75*, 014304. [CrossRef]

42. Espinosa, V.; Sánchez-Morcillo, V.J.; Staliunas, K.; Pérez-Arjona, I.; Redondo, J. Subdiffractive propagation of ultrasound in sonic crystals. *Phys. Rev. B* **2007**, *76*, 140302. [CrossRef]

43. Peiró-Torres, M.P.; Ferri, M.; Godinho, L.M.; Amado-Mendes, P.; Vea Folch, F.J.; Redondo, J. Normal incidence sound insulation provided by Sonic Crystal Acoustic Screens made from rigid scatterers–assessment of different simulation methods. *Acta Acust.* **2021**, *5*, 28. [CrossRef]

44. Taflove, A.; Brodwin, M.E. Numerical solution of steady-state electromagnetic scattering problems using the time-dependent Maxwell's equations. *IEEE Trans. Microw. Theory Tech.* **1975**, *23*, 623–630. [CrossRef]

45. Catapane, G.; Magliacano, D.; Petrone, G.; Casaburo, A.; Franco, F.; De Rosa, S. Semi-analytical estimation of Helmholtz resonators' tuning frequency for scalable neck-cavity geometric couplings. *CEAS Aeronaut. J.* **2022**, *13*, 797–808. [CrossRef]

46. Sanchis, L.; Cervera, F.; Sánchez-Dehesa, J.; Sánchez-Pérez, J.V.; Rubio, C.; Martínez-Sala, R. Reflectance properties of two-dimensional sonic band-gap crystals. *J. Acoust. Soc. Am.* **2001**, *109*, 2598–2605. [CrossRef] [PubMed]

47. Mbailassem, F.; Gourdon, E.; Leclère, Q.; Redon, E.; Cambonie, T. Sound absorption prediction of linear damped acoustic resonators using a lightweight hybrid model. *Appl. Acoust.* **2019**, *150*, 14–26. [CrossRef]

48. Kampinga, R. Viscothermal Acoustics Using Finite Elements, Analysis Tools for Engineers. PhD Thesis, University of Tweente, Enschede, The Netherlands, 2010.